# A Versatile Detection Method for Various Contrast Enhancement Manipulations

Xiuli Bi, Yixuan Shang, Bo Liu, *Member, IEEE*, Bin Xiao, Weisheng Li, *Member, IEEE*, and Xinbo Gao, *Senior Member, IEEE*

***Abstract*—Contrast enhancement manipulation is a common method to improve the visual effect of an image. Meanwhile, it can also be considered a type of global image forgery because it changes the image's visual appearance without alerting its semantics. Moreover, for local image forgery, a tampered image may be composited by images with different contrast enhancement manipulations or post-processed by a contrast enhancement manipulation to conceal the trails of tampering. Therefore, contrast enhancement manipulation detection is critical to global image forgery detection. The existing methods can only detect a particular type of contrast enhancement manipulation, such as gamma correction or histogram equalization. To break this limitation, we propose the zero-gap spans (ZGS) as the fingerprint to explore the traces of contrast enhancement manipulations. Based on ZGS, various contrast enhancement manipulations can be distinguished by a simple classification method at image-level and patch-level; different gamma corrections can be identified, and their gamma value can be estimated. Experimental results indicate that the proposed ZGS-based classification method can achieve and maintain good classification performance under different cases (gamma correction, simple histogram equalization, modified histogram equalization techniques). Meanwhile, ZGS can estimate the gamma value with the mean squared error (MSE) below 0.1156. For the local forgery images, the proposed ZGS also can be utilized to locate the regions with different contrast enhancement manipulations.**

***Index Terms*—Global forgery detection, contrast enhancement manipulation, gamma correction, histogram equalization, ZGS.**

## I. Introduction

NOWADAYS, creating forgeries on an image can be done by just clicking a key in image-editing software and many Apps, which is very easy and does not require professional skills. Meanwhile, the rapid development of the Internet and social platforms has led to the widespread dissemination of these fake images, which may mislead people's perceptions or affect the judgment of decision-makers on some critical occasions. Since these fake images have caused many serious public opinion issues, it is more and more necessary to authenticate the images from the perspective of information security.

So far, the proposed image authentication approaches can be generally classified into two classes: the active methods and the passive methods. The active methods verify images using the previously inserted information in the original images, for instance, watermarking [1]. The passive methods are blind methods without the help of any previously inserted information and only conduct authentications on observed images. Over the last two decades, many passive authentication methods have been proposed, which are usually divided into local forgery detection and global forgery detection. Most of them were proposed for detecting the local image forgery. The local forgery is to tamper with the semantic content of an image by changing some parts of the image, such as copy-move forgery [2], [3] and splicing forgery [4], [5], [6]. For detecting the local image forgery, these detection methods generally explore the tampered regions by calculating the difference or similar properties among image regions. However, the detection methods for global image forgery are rare. The typical global image manipulations [7] include filtering operation [8], [9], [10], [11], JPEG compression [12], [13], [14], [15], [16], [17], and contrast enhancement [18], [19], [20], [21], [22]. From these image manipulations, we can see the global image forgery changes an image's visual appearance without alerting the image's semantics. Since only the global properties of the images are modified, it is more complicated to distinguish the global forgery images from the original images by exploring the potential regularities.

Gamma correction and histogram equalization attract the most attention in previous research on contrast enhancement manipulation as global image forgery. Due to simplicity and effectiveness, they are usually used to modify the visual effect of an image and as the post-processing of the local image forgery to conceal the trails by blurring the difference between the tampered region and the non-tampered region. In gamma correction and histogram equalization, the pixel value of an input image is mapped to the new pixel value by a specific mapping function. Since the specific mapping function will leave the trails on the histograms of output images, the statistical characteristics of the histograms

Manuscript received 4 March 2022; revised 10 June 2022 and 28 July 2022; accepted 4 September 2022. Date of publication 6 September 2022; date of current version 6 February 2023. This work was supported in part by the National Key Research and Development Project under Grant 2019YFE0110800 and Grant 2016YFC1000307-3, in part by the National Natural Science Foundation of China under Grant 62172067 and Grant 61976031, and in part by the National Major Scientific Research Instrument Development Project of China under Grant 62027827. This article was recommended by Associate Editor T. Akilan. *(Corresponding authors: Bo Liu; Bin Xiao.)*

The authors are with the Department of Computer Science and Technology, Chongqing University of Posts and Telecommunications, Chongqing 400065, China (e-mail: bixl@cqupt.edu.cn; s190231114@stu.cqupt.edu.cn; boliu@cqupt.edu.cn; xiaobin@cqupt.edu.cn; liws@cqupt.edu.cn; gaoxb@cqupt.edu.cn).

Color versions of one or more figures in this article are available at https://doi.org/10.1109/TCSVT.2022.3204789.

Digital Object Identifier 10.1109/TCSVT.2022.3204789

can be regarded as a sign of these contrast enhancement manipulations.

Based on this idea, some detection methods using the statistical characteristics of the histogram have been proposed [18], [19], [20], [21], [22]. Stamm and Liu [18] detect histogram equalization by considering the strength of frequency components in the image histogram and detect local contrast enhancement. Yuan [19] models the gray-level cumulative distribution of histogram-equalized images as a discrete identity function and then matches it with observed gray-level cumulative distribution to identify the use of global histogram equalization. Akhtar and Khan [20] propose a method that can detect forged images saved in JPEG format after histogram equalization manipulation. Cao *et al.* [21] explore statistical abnormity on image grayscale histograms caused by gamma correction. In [22], they continue their work on global and local gamma correction in an image that was previously JPEG compressed. Since the discrimination power of their proposed features is not good enough, each existing method can detect only one type of contrast enhancement manipulation, either histogram equalization [18], [19], [20] or gamma correction [21], [22].

In the actual scene, the forgery is far more complicated than analysis. If a method only can detect one type of contrast enhancement manipulation, 1) it cannot distinguish these common types of contrast enhancement manipulations, which will limit the application of the detection method in real scenes; 2) when different types of contrast enhancement manipulations are performed in both tampered and non-tampered regions simultaneously, it will be impossible to distinguish them; 3) when we need to know the degree of contrast enhancement for accomplishing the further tasks, such as image restoration, it cannot provide any clues.

To break this limitation, we propose a versatile detection method for various contrast enhancement manipulations in this paper. Our main contributions in this paper are listed below.

- ZGS is proposed as the only feature to discriminate various types of contrast enhancement manipulations.
- Based on ZGS, we propose a simple classification method that can distinguish various contrast enhancement manipulations at image-level and patch-level.
- We further explore the clues of gamma correction manipulation showed by ZGS, and then propose a gamma value estimation method.

Our method improves the practicability of the detection method for global contrast enhancement manipulations in real situations because of its versatility. It can handle more various cases of locally forged images that are related to contrast enhancement manipulations. Moreover, it can also help further tasks required to know the gamma value used in gamma correction. The comparison between the discrimination power of ZGS and other histogram-based features used in existing methods is summarized in Table I.

The rest of this paper is organized as follows. The fingerprint of contrast enhancement manipulation is analyzed in Section II. The proposed detection method for contrast enhancement manipulations is presented in Section III. Section IV verifies the effectiveness of the proposed method. Finally, we conclude our work in this paper in Section V.

TABLE I

SUMMARY OF THE DISCRIMINATION POWER OF ZGS AND THE OTHER HISTOGRAM-BASED FEATURES USED IN EXISTING METHODS. ORG: ORIGINAL IMAGES; HE: HISTOGRAM EQUALIZATION; GC: GAMMA CORRECTION; GE: GAMMA VALUE ESTIMATION

| | zero-gap numbers | zero-gap distribution | ZGS |
|---|---|---|---|
| ORG+HE/GC | ✓ | ✓ | ✓ |
| ORG+HE+GC | | ✓ | ✓ |
| ORG+HE+GC+GE | | | ✓ |

## II. FINGERPRINT OF CONTRAST ENHANCEMENT MANIPULATIONS

Contrast enhancement manipulations aim to adjust the contrast of an image, and the different types of contrast enhancement manipulations have different rules of adjustment. In previous research, since contrast enhancement manipulations considered as global image forgery mainly include gamma correction and histogram equalization, we first review them.

### A. Review of Contrast Enhancement Manipulations

Gamma correction is originally used to encode and decode luminance by power-law function in various devices that produce images and videos, and the power-law function is

$$y(x) = x^{\gamma} \quad (\gamma > 0), \tag{1}$$

where $x \in [0, L-1]$ represents the pixel intensity of the input image, and $y(x)$ is the corresponding pixel intensity after gamma correction. $\gamma$ is the parameter of gamma correction, and various devices own different $\gamma$. When $\gamma > 1$, the output pixel intensity $y(x)$ is lower than the input pixel intensity $x$. Otherwise, the output pixel intensity $y(x)$ is higher than the input pixel intensity $x$.

Unlike gamma correction, histogram equalization attempts to increase the contrast of a digital image by generating a mapping, making the intensities of the output image more evenly distributed in the histogram. The mapping is accomplished using

$$T(x) = round\left[(L-1) \times \frac{cdf(x) - cdf_{min}}{M \times N - cdf_{min}}\right], \tag{2}$$

where $M \times N$ is the size of the input image; $cdf(x)$ is the number of pixels whose intensity value is equal or less than $x$; $cdf_{min}$ is the number of pixels with the minimum non-zero intensity value in the image; $L$ is the number of possible intensity levels; $T(x)$ represents the output pixel intensity for input pixel intensity $x$ after histogram equalization transformation $T$.

### B. Zero-Gaps Left by Contrast Enhancement Manipulations

Since gamma correction or histogram equalization alters the pixel intensities of an image by the above mapping rules, they will leave certain traces on the image's histogram. For gamma

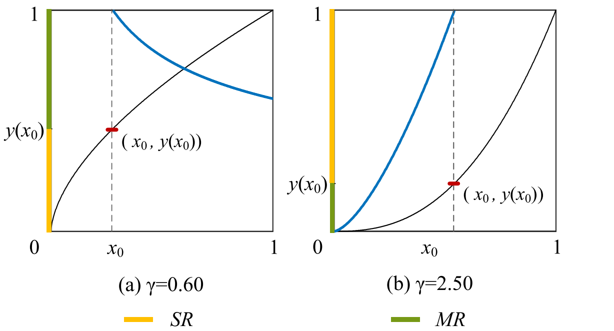


Fig. 1. Two power-law functions with different parameters $\gamma$ and their stretched and merged range. The black lines are power-law functions $y(x) = x^{\gamma}$ and the blue lines are their first derivatives $y'(x)$. $x_0$ is the point where $y'(x_0) = 1$.

correction, no matter what kind of parameter $\gamma$, the slope of each point on the power-law function $y(x)$ is different. The slope can be calculated by the first derivative $y'(x)$ shown as blue lines in Fig. 1. According to the properties of power-law function and Lagrange Mean Value Theorem [23], there exists a point $(x_0, y(x_0))$ such that $y'(x_0) = 1$. Since the power-law function $y(x)$ is a monotonous function, there is a continuous interval where $y'(x) > 1$. In this interval, the input pixel intensity will be dispersively mapped to the output pixel intensity range, which will cause disappearing bins in the output image's histogram. Based on this phenomenon, [21], [22] name the disappearing bins as zero-gaps, which satisfy

$$b_k = 0, \min\{b_{k-1}, b_{k+1}\} > \tau, \tag{3}$$

where $b_k$ is the height of the $k$-th bin of the image's normalized histogram. The first sub-equation assures that the corresponding bin is null, and the second sub-equation keeps the neighboring bins larger than a small threshold $\tau$.

By counting the number of the defined zero-gaps, [21], [22] proposed methods to detect gamma correction. However, their proposed method can only distinguish the original images and the images manipulated by gamma correction, and they did not further explore the phenomenon of zero-gaps.

In this paper, we analyze this phenomenon in more depth. For the power-law function $y(x)$, when $y'(x) > 1$, the input pixel intensity will be dispersively mapped to the output pixel intensity range; when $y'(x) < 1$, the input pixel intensity are intensively mapped to the output pixel intensity range. Therefore, the output pixel intensity range can be separated by Stretched Range ($SR$) and Merged Range ($MR$). As shown in Fig. 1-(a), when $\gamma < 1$, the output pixel intensity range can be separated as in Eq. 4.

$$\begin{aligned} SR &: [0, y(x_0)]; \\ MR &: [y(x_0), 1]. \end{aligned} \tag{4}$$

As shown in Fig. 1-(b), when $\gamma > 1$, the output pixel intensity range can be separated as in Eq. 5.

$$\begin{aligned} SR &: [y(x_0), 1]; \\ MR &: [0, y(x_0)]. \end{aligned} \tag{5}$$

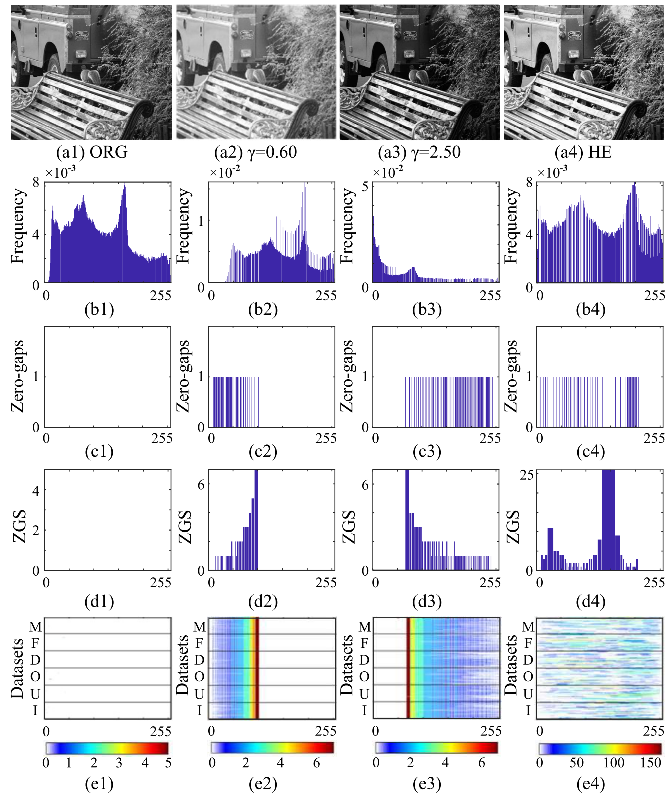


Fig. 2. From left to right: the original image; gamma correction $\gamma = 0.60$; gamma correction $\gamma = 2.50$; histogram equalization. From top to bottom: the observed images; the histograms (figures should be zoomed in to see the zero-gaps); the zero-gaps of the histograms; the distribution of the ZGS; the distribution of ZGS on different datasets (a vertical line visualizes the ZGS of an image: the color represents the value of ZGS. M: MFC; F: FR; D: MD; O: COCO; U: UCUS; I:UCID. See Table. III for details). The $x$-axis is the pixel value.

When an image (as shown in Fig. 2-(a1)) is operated by gamma corrections with different $\gamma$, since the zero-gaps only occur in $SR$, it can be observed that when $\gamma < 1$, the zero-gaps distribute on the left side of the histogram in Fig. 2-(c2), and they appear on the right side of the histogram when $\gamma > 1$ in Fig. 2-(c3). As shown in Fig. 2-(c4), since the image pixel distribution is more uniform after histogram equalization, the distribution of zero-gaps is unpredictable and relatively uniform.

### *C. ZGS Fingerprint of Contrast Enhancement Manipulation*

We can see above, using the distribution of zero-gaps can roughly infer the range of $\gamma$ of the power-law function $y(x)$ in gamma correction. Practically, the probability of zero-gaps occurrence is also determined by the slope of the power-law function $y(x)$: the zero-gaps in an interval where the absolute value of the slope is large has a higher occurrence chance because of a stronger stretching power caused by the power-law function $y(x)$. Therefore, when approaching the point $y(x_0)$ where the first derivative $y'(x)$ equals 1 in the stretched area $SR$, as the stretching power becomes weaker, the number of zero-gaps is smaller, resulting in larger adjacent distances between two zero-gaps.

For describing this phenomenon, we define the distances between two neighboring zero-gaps as ZGS. Supposing $K$ as a

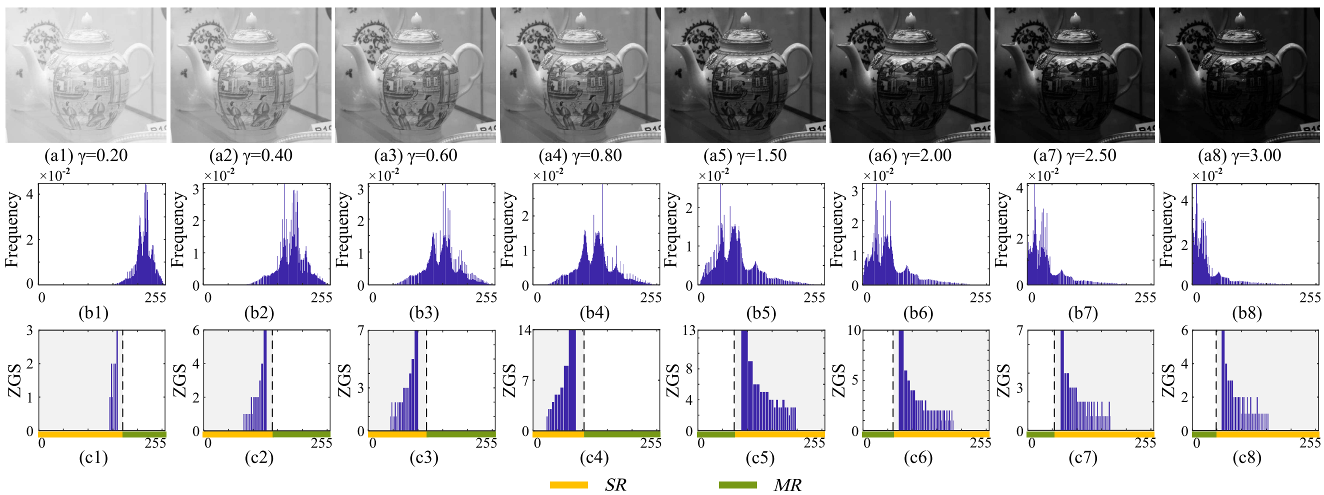


Fig. 3. From left to right: the gamma corrections with $\gamma$ equals 0.20, 0.40, 0.60, 0.80, 1.50, 2.00, 2.50, 3.00, respectively. From top to bottom: the observed images; the histograms and the figures should be zoomed in to see the zero-gaps; the distribution of the ZGS. The $x$-axis is the pixel value.

sorted set containing all position index $k$ of zero-gaps in Eq. 3 in the histogram in ascending order. The ZGS fingerprint $\mathbf{Z}$ is then generated as a 256-dim feature vector by Eq. 6, which corresponds to the 256 bins of the histogram.

$$\mathbf{Z}(j) = \begin{cases} K_{i+1} - K_i - 1, & \text{if } j \in (K_i, K_{i+1}) \\ 0, & \text{otherwise,} \end{cases} \tag{6}$$

where $i$ is the $i$-th element in set $K$, $i \in \{1, \ldots, 254\}$. Eq. 6 counts the number of bins between two zero-gaps in a histogram, and this value is recorded in the corresponding index of the ZGS fingerprint $\mathbf{Z}$.

The ZGS distribution can be viewed in the $d^{th}$ row of Fig. 2. We can observe, as the stretching power declines when approaching $y(x_0)$ in $SR$, the value of ZGS gradually becomes higher, and the largest values appear around $y(x_0)$. Therefore, ZGS has two characters:

- the ZGS distribution can reflect various types of contrast enhancement manipulations, which is similar to the distribution of zero-gaps;
- the value of ZGS can infer the stretching power of the power-law function $y(x)$, which actually corresponds to the slope of the power-law function $y(x)$.

In order to evaluate the two characters of ZGS, we randomly selected 300 images from each of six public datasets and performed contrast enhancement manipulations, including histogram equalization, gamma correction where $\gamma = 0.60, 2.50$. Then we extracted ZGS and show them in a gathered form in Fig. 2-(e1) (e4): a horizontal line denotes a ZGS distribution of an image, and its color represents the ZGS value. The distinction between different contrast enhancement manipulations from the gathered ZGS distribution is clear: almost no ZGS appear in the original images in Fig. 2-(e1); no apparent regular pattern presents for images after histogram equalization in Fig. 2-(e2); the ZGS distribution is denser on the left side of the pixel value range when $\gamma < 1$ in Fig. 2-(e2); it is denser on the right side of the pixel value range when $\gamma > 1$ in Fig. 2-(e3). Although the content of images in datasets is different, their ZGS distribution after the same gamma correction is quite similar. Take $\gamma = 0.60$ for example: their ZGS value gradually increases from left to right and decreases to zero right after the peak. And it is affected by the slope of the power-law function $y(x)$. Therefore, we can use ZGS distribution as the fingerprint left by gamma correction to estimate $y(x)$.

### D. Preliminary Classification Based on ZGS

Directly based on the proposed ZGS, we can classify the various types of contrast enhancement manipulations. For an image, we performed quadratic curve fitting $g$ with mean square error as the fitting metric on the non-zero part of each ZGS and selected the median position $a$, $b$, and $c$ in the largest, second-largest spans, third-largest spans. Then we determined the slope of $g'(a)$, $g'(b)$, and $g'(c)$ of the three points on the curve. The ZGS distribution and the fitted curves of different manipulations are shown in the first row of Fig. 4. In the second row of Fig. 4, the slope at $a$, $b$, $c$ has an obvious pattern after different manipulations. There are almost no zero-gaps in the original image, so ZGS does not exist. When $\gamma < 1$, $g'(a)$, $g'(b)$ and $g'(c)$ are in decending order, and when $\gamma > 1$ they are in ascending order. Since ZGS has no such order after histogram equalization, $g'(a)$, $g'(b)$, and $g'(c)$ show no numeric order.

A simple classification experiment can be conducted according to this simple rule on six datasets, including histogram equalization and gamma corrections with 14 parameters between 0.20 and 5.00. Table II shows the results in $CCPs$ defined by Eq. 17 of the four-class classification. The good performance of the simple classification rule proves that ZGS can well describe the patterns left by different types of contrast enhancement manipulations.

## III. Detection of Contrast Enhancement Manipulations

Based on the above exploration of ZGS, we utilize its two characters further, propose one method to classify various

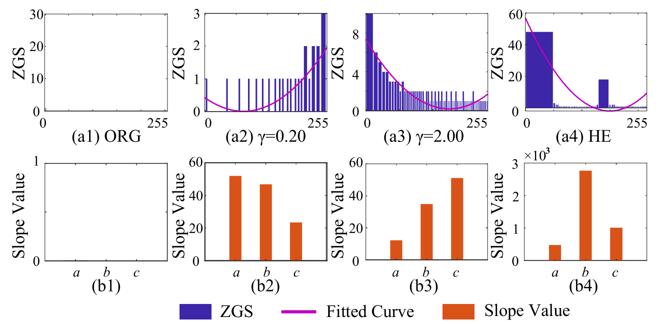


Fig. 4. ZGS histogram of the original image, images after gamma corrections, and histogram equalization. The first row is ZGS and the corresponding fitted quadratic curves, and the $x$-axis is the pixel value. The second row is the slopes of $a$, $b$, $c$ on the fitted curve; $a$, $b$, $c$ denote the median position in the largest, second-largest spans, third-largest spans in the ZGS histogram respectively.

TABLE II

EXPERIMENTAL RESULTS IN $CCPs$ OF THE FOUR-CLASS CLASSIFICATION FOR ORIGINAL IMAGE, HISTOGRAM EQUALIZATION AND TWO CLASSES OF GAMMA CORRECTION ($\gamma_1$, $\gamma_2$) BY THE SLOPE RULE

| ORG+HE+$\gamma_1$+$\gamma_2$ | | Dataset | | | | | |
|---|---|---|---|---|---|---|---|
| $\gamma_1$ | $\gamma_2$ | UCID | UCUS | COCO | MD | FR | MFC |
| 0.20 | 5.00 | 94.73 | 97.02 | 95.76 | 95.71 | 96.10 | 93.06 |
| 0.30 | 3.33 | 95.78 | 97.86 | 96.91 | 96.79 | 96.83 | 94.66 |
| 0.40 | 2.50 | 96.41 | 98.15 | 97.29 | 97.22 | 97.05 | 95.39 |
| 0.50 | 2.00 | 96.60 | 98.39 | 97.57 | 97.47 | 97.18 | 95.68 |
| 0.60 | 1.67 | 96.38 | 98.39 | 97.45 | 97.34 | 97.03 | 95.48 |
| 0.70 | 1.43 | 95.29 | 97.74 | 97.19 | 96.85 | 96.83 | 95.00 |
| 0.80 | 1.25 | 93.72 | 97.44 | 96.73 | 96.17 | 96.30 | 94.13 |

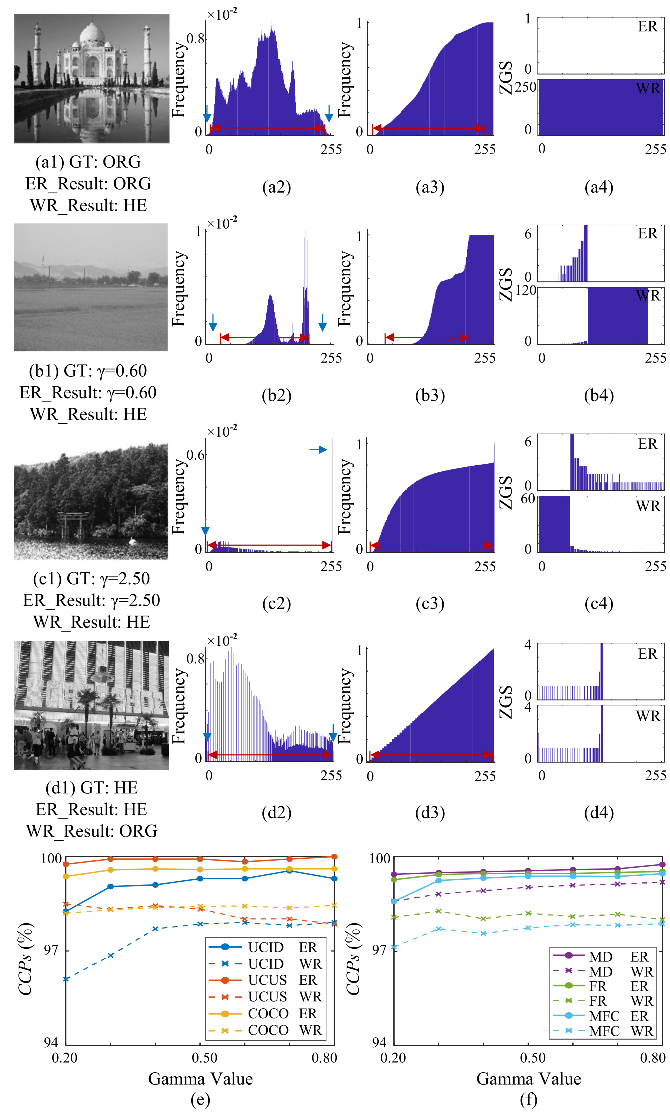


Fig. 5. Adaptive effective range selection and its effect on classification result. The red arrow shows the selected effective range, and the blue arrow points out the bins or intervals not included in the range. The $x$-axis is the pixel value. From left to right in the first four rows: the observed images; the histogram of the observed images; the cumulative distribution of the observed images; the ZGS distribution from ER and WR. From top to bottom in the first four rows: the original image; gamma correction $\gamma = 0.60$; gamma correction $\gamma = 2.50$; histogram equalization. (e)(f) The classification accuracy in $CCPs$ from ER and WR on different datasets. ER: effective range; WR: whole range; GT: ground truth; WR_Result: the classification result from the whole range; ER_Result: the classification result from the adaptively selected effective range.

contrast enhancement manipulations and another method to estimate the parameter $\gamma$ in gamma correction.

### A. Classifying Various Contrast Enhancement Manipulations by ZGS Fingerprint

The above preliminary classification shows the proposed ZGS has good discrimination power, which can be further used with proper classifiers to discern various contrast enhancement manipulations. The support vector machine (SVM) classifier is trained using the extracted ZGS fingerprints $\mathbf{Z}$ from the training set and then is used to classify the original images and the different manipulations. From the classification result, we observed that the false results are related to ZGS extracted at both ends of histograms. Some examples are shown in Fig. 5, and it can be seen that these zero-gaps at both ends of the histograms are not caused by the stretching effect of the mapping function. Therefore, feature extraction including both ends of histograms will reduce the descriptive ability of ZGS as the fingerprint of contrast enhancement manipulations. Previous manipulated image detection methods [18], [19], [20], [21], [22] perform feature extraction from a whole gray-level range, thus achieving reduced classification accuracy without adequately handling the issue.

To solve this issue, we need to locate the gray-pixel range to reflect the effect of the mapping function. For an image, only if its cumulative distribution rises is it possible to yield zero-gaps caused by the stretching effect of the mapping function. In order to find this effective range, the slope $cdf'(t)$ of point $t$ on the curve of the cumulative distribution $cdf(x)$ is defined as

$$cdf'(t) = \frac{cdf(t+1) - cdf(t-1)}{x(t+1) - x(t-1)}, \tag{7}$$

where $x(t) \in \{0, 1, \ldots, 255\}$ is the pixel intensity of point $t$. The starting gray-level $R_s$ and the end gray-level $R_e$ of the selected effective range are determined by Eq. 8 and Eq. 9.

$$R_s = \min\left\{x(t)\ \middle|cdf'(t) \neq 0, cdf(t) \neq 0\right\}; \quad (8)$$

$$R_e = \min\left\{x(t)\ \middle|cdf'(t) < \delta, cdf(t) \neq 0\right\}. \quad (9)$$

If $\delta$ is set too large, the selected effective range for extracting ZGS fingerprint **Z** will become shorter, and the useful intensities will lose, making the extracted ZGS insufficient to represent the fingerprint of contrast enhancement manipulations. We conducted experiments and found that the proper value of $\delta$ is 0.003. It should be noted that this adaptive effective range selection process does not change the length of the ZGS fingerprint **Z**. Instead, we extract ZGS in a range defined by Eq. 8 and Eq. 9. After adaptive effective range has been

After extracting the ZGS fingerprint **Z** refined by adaptive effective range selection, we choose SVM to discern manipulations for its excellent generalization ability and good classification performance on small sample datasets. To implement multi-classification, we choose the LibSVM library [24] which adopts a One-versus-One (OVO) strategy. As for the RBF kernel parameters, the grid search and cross-validation are used to obtain the best parameters. Fig. 6 depicts the flowchart of our proposed classification method based on the ZGS extraction process with adaptive effective range selection.

In order to show the influence of the range selection, we conducted three-class classification experiments, including original images, histogram equalization, and gamma correction from 0.20 to 0.80 on six datasets. Using the whole range of the image histogram to extract ZGS has worse performance than extracting ZGS from an effective range in a histogram, which is shown in Fig. 5-(d)∼(e).

### B. Gamma Value Estimation by ZGS Fingerprint

In addition to classifying various contrast enhancement manipulations, ZGS can also be used to perform gamma value estimation. The ZGS fingerprint **Z** provides necessary clues for gamma value estimation.

The first clue is the position of the maximum value in the ZGS fingerprint **Z**, and the position is related to $\gamma$. Since the maximum value appears round the position $y(x_0)$, we analyse the relationship between $y(x_0)$ and $\gamma$. Get the first derivative of the power-law function in Eq. 1:

$$y'(x) = \gamma x^{\gamma-1}. \quad (10)$$

Let $y'(x) = 1$ and we get its solution $x_0$ in Eq. 11:

$$x_0 = e^{\frac{\ln\gamma}{1-\gamma}}. \quad (11)$$

Substitute $x_0$ into Eq. 1 and obtain Eq. 12:

$$y(x_0) = e^{\frac{\gamma}{1-\gamma}\ln\gamma}. \quad (12)$$

Eq. 12 clearly reveals the relationship between $y(x_0)$ and the parameter $\gamma$ under ideal condition. This relationship can be observed in the ZGS distribution in Fig. 3-(c1)∼(c4): since $y(x_0)$ monotonously decreases regarding $\gamma$ in Eq. 12 (shown in Fig. 7-(a)), as $\gamma$ increases from 0.2 to 0.8, $y(x_0)$ decreases. It consequently makes the maximum value in the ZGS distribution move to the left. This happens when $\gamma > 1$ in Fig. 3-(c5)∼(c8) as well: when $\gamma$ increases from 1.5 to 3.0, the maximum value move to the left, where $y(x_0)$ is smaller. Since the maximum value in **Z** appears around $y(x_0)$ but not the exact position of $y(x_0)$, we cannot directly solve Eq. 12 to obtain the value of $\gamma$.

The second clue is the maximum value in the ZGS fingerprint **Z**, which is also determined by $\gamma$. We consider a small interval $\Delta x$ around $x_0$, where $y'(x_0) = 1$. The slope around $x_0$ is then obtained by Eq. 13.

$$y'(x_0; \Delta x) = \gamma\ (x_0 + \Delta x)^{\gamma-1}. \quad (13)$$

We substitute Eq. 11 into Eq. 13 and get Eq. 14.

$$y'(\gamma; \Delta x) = \gamma\left(e^{\frac{\ln\gamma}{1-\gamma}} + \Delta x\right)^{\gamma-1}. \quad (14)$$

In Eq. 14, when $\gamma < 1$, since $SR$ is on the left side of $x_0$, we set $\Delta x < 0$, and we set $\Delta x > 0$ when $\gamma > 1$ since $SR$ is on the right side of $x_0$. The image of Eq. 14 can be seen in Fig. 7-(b). It shows that when $\Delta x < 0$, Eq. 14 is a set of monotonously decreasing functions: when $\gamma$ rises, the slope $y'(\gamma; \Delta x)$ decreases, resulting in producing fewer zero-gaps and consequently yielding larger value in the ZGS distribution. The Fig. 3-(c1)∼(c4) verify such conclusion. On the contrary, when $\Delta x > 0$, functions in Eq. 14 are monotonously increasing: as $\gamma$ increases, the slope $y'(\gamma; \Delta x)$ rises, leading to more zero-gaps, and the maximum value decreases consequently. The Fig. 3-(c5)∼(c8) support the analysis above.

Based on the analysis above, the parameter $\gamma$ affects the maximum value and their positions in the ZGS fingerprint **Z**. We can therefore use these two variables to infer $\gamma$ via two-variable regression. The first variable $S_1$ records the position of the maximum value in **Z**. Since there may be more than one maximum value, we use the most right-side one when $\gamma < 1$ and the most left-side one when $\gamma > 1$. Formally, the $S_1$ can be obtained from the ZGS fingerprint **Z** by Eq. 15.

$$S_1 = \begin{cases} \max\{\arg\max\limits_i \mathbf{Z}(i)\} & \text{if } \gamma < 1 \\ \min\{\arg\max\limits_i \mathbf{Z}(i)\} & \text{if } \gamma > 1 \end{cases}. \quad (15)$$

The second variable $S_2$ is the maximum value in the ZGS fingerprint **Z**, as shown in Eq. 16.

$$S_2 = \max \mathbf{Z}(i). \quad (16)$$

Then, the process of estimate the parameter $\gamma$ is described in **Algorithm 1** and the coefficients $\alpha_1, \alpha_2, \beta_1, \beta_2, \theta_1, \theta_2$ can be obtained by training on image datasets.

## IV. Experiments and Analysis

This section presents extensive experiments and experimental results to verify the effectiveness of our proposed method in discrimination of manipulation, estimation of the parameter in gamma correction, and detecting local image manipulations. In Section IV-A, the datasets and the evaluation

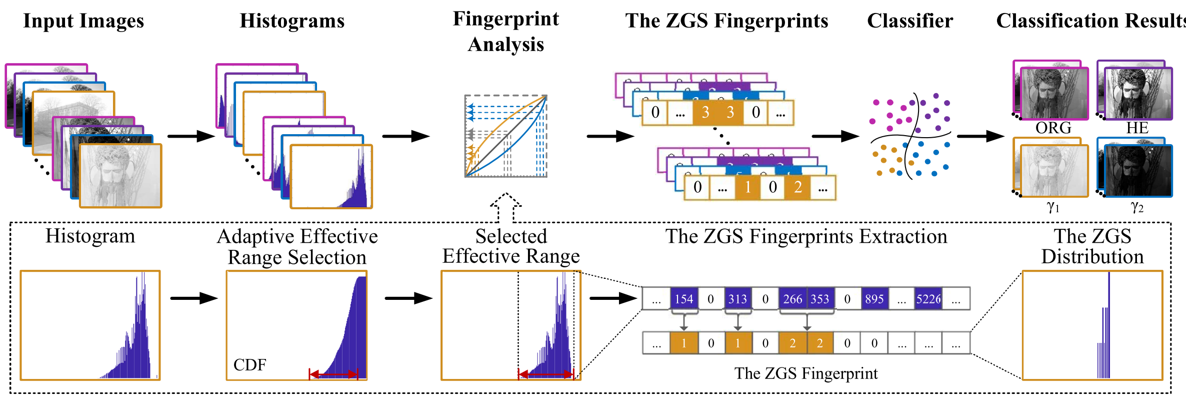


Fig. 6. Framework of the proposed method to classify various contrast enhancement manipulations with adaptive effective range selection. CDF: Cumulative distribution function.

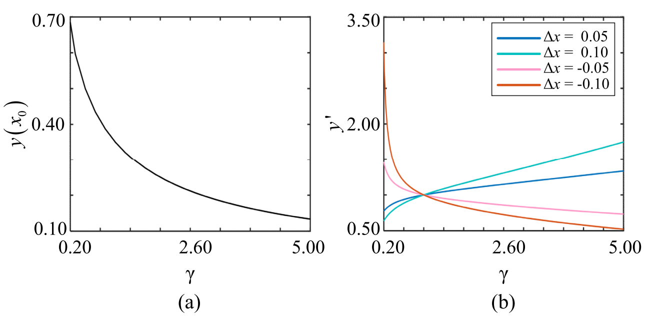


Fig. 7. Images of Eq. 12 and Eq. 14. (a) The relationship between $y(x_0)$ and parameter $\gamma$ in Eq. 12. (b) The relationship between $y'$ and $\gamma$ in a small interval $x_0 + \Delta x$ in Eq. 14.

**Algorithm 1** Estimate the Parameter $\gamma$ in Gamma Correction

**Input**: ZGS feature set $T$, coefficients $\alpha_1, \alpha_2, \beta_1, \beta_2, \theta_1, \theta_2$.
**Output**: Gamma correction estimate value $\hat{\gamma}$.

**for** each $\mathbf{Z} \in T$ **do**
  Fit the non-zero interval of $\mathbf{Z}$ using quadratic curve $g$;
  Obtain the index of median position $a$, $b$, $c$ in the largest, the second-largest and the third-largest spans;
  Compute the slope values $g'(a)$, $g'(b)$ and $g'(c)$;
  **if** $g'(a) > g'(b) > g'(c)$ **then**
    Compute $S_1 = \max\{\arg\max(\mathbf{Z})\}$;
    Compute $S_2 = \max(\mathbf{Z})$;
    Compute $\hat{\gamma} = \alpha_1 \ln S_1 + \beta_1 \ln S_2 + \theta_1$;
  **end if**
  **if** $g'(a) < g'(b) < g'(c)$ **then**
    Compute $S_1 = \min\{\arg\max(\mathbf{Z})\}$;
    Compute $S_2 = \max(\mathbf{Z})$;
    Compute $\hat{\gamma} = \alpha_2 \ln S_1 + \beta_2 \ln S_2 + \theta_2$;
  **end if**
**end for**
Return $\hat{\gamma}$

metric are introduced. The evaluation of the proposed classification method and comparisons are discussed and explored in Section IV-B. Section IV-C presents the gamma value estimation. The analysis of robustness and the application of our method to image authentication are discussed in Section IV-D and IV-E respectively. The experiments were performed on the Intel (R) Core (TM) i7-4790 CPU @ 3.60GHz PC (Matlab 2018a, win10) platform.

### A. Datasets and Evaluation Metric

*1) Datasets:* The experiments use the following six datasets: UCID [25], UCUS [26], COCO [27], MD, Fantastic Reality (FR) [28], and MFC [29]. The specifications of these datasets is summarized in Table III. The UCID uncompressed color image library includes natural scenery, buildings, people, indoor and outdoor scenes. The UCUS color image dataset is a collection of JPEG images of different sizes collected from different sources, with a total of 840 images, and includes multiple resolutions from $520 \times 358$ to $3648 \times 2736$. The third dataset is a collection of 3915 JPEG color images randomly selected from the COCO dataset released by Microsoft, including various resolutions from $333 \times 240$ to $640 \times 640$. In order to detect JPEG format, TIFF format, and images of different resolutions simultaneously, we combined these three original datasets into a merged dataset MD with a total of 6093 images for experiments. FR [28] includes authentic and spliced images for various scenes with pixel-level ground truth masks, and we only randomly selected 2000 real images for the experiment. The MFC dataset is a large-scale benchmark dataset for media forensic challenge evaluation, and 4,316 original images were selected randomly for experiments.

*2) Evaluation Metric:* For testing the performance of our proposed classification method, the experiment uses the correct classification percentages ($CCPs$) as the evaluation metric to verify the effectiveness of the classification method, and the definition is

$$CCPs = \frac{\text{the number of correctly classified images}}{\text{the total number of classified images}} \times 100\%. \tag{17}$$

Besides, the confusion matrix is used for evaluation, which contains information about groundtruth and predicted

TABLE III
SPECIFICATIONS OF THE SIX DATASETS USED IN THE EXPERIMENT

| Dataset | Resolution | Format | Total | Training | Testing |
|---|---|---|---|---|---|
| UCID [25] | 512×384 | TIFF | 1338 | 669 | 669 |
| UCUS [26] | 520×385~3648×2736 | JPEG | 840 | 420 | 420 |
| COCO [27] | 333×240~640×640 | JPEG | 3915 | 1957 | 1958 |
| MD | 333×240~3648×2736 | TIFF, JPEG | 6093 | 3046 | 3047 |
| FR [28] | 800×69~6000×4000 | JPEG | 2000 | 1000 | 1000 |
| MFC [29] | 150×51~10810×4029 | JPEG | 4316 | 2158 | 2158 |

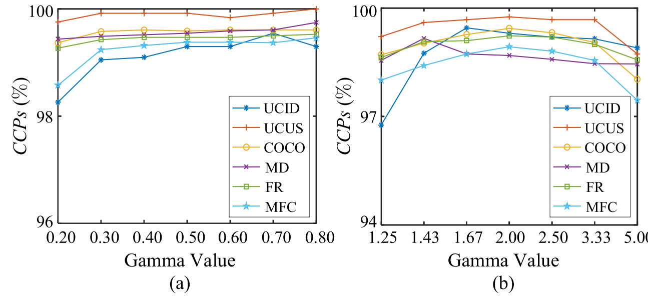


Fig. 8. Three-class classification results in $CCPs$ in the same dataset. (a) The experimental results classifying original images, histogram equalization, and gamma correction when $\gamma < 1$. (b) The experimental results classifying original images, histogram equalization, and gamma correction when $\gamma > 1$.

classifications and is usually used to evaluate the performance of a method intuitively.

### B. Evaluations of the Classification Method

*1) Experiments Under the Same Dataset:* In this section, the experiments are carried out to estimate the performance of the proposed classification method to distinguish original images, images after histogram equalization, and images after gamma correction. The training and testing set in this section are from the same dataset. And the number of training and testing images are shown in Table. III.

The three-class classification experiment includes original images, images after histogram equalization, and images after gamma correction. In the case of $\gamma < 1$, we selected parameter $\gamma$ from 0.20 to 0.80 with an interval of 0.10. While $\gamma > 1$, the reciprocals of the parameters in the former case are used. Fig. 8 (a) and (b) show the experimental results with different gamma values. We can see that the proposed classification method can successfully distinguish the three classes with good performance. No matter the images in JPEG or TIFF format, or the merged dataset in JPEG and TIFF format, it does not affect the performance of the proposed classification method. It can be seen that when the parameter $\gamma$ takes the extreme value, such as $\gamma = 0.20$ and $\gamma = 5.00$, the classification performance is slightly affected. This is because the extreme value of $\gamma$ greatly changes the image, concentrating image pixels in a very low or a very high intensity range, which affects the extraction of fingerprint features. When $\gamma = 1.25$, the change of intensity caused by gamma correction is very slight, so there is a little difference in the fingerprint feature between the original and operated images. However, the proposed classification method can still distinguish the manipulations successfully.

The experiments above only include one gamma correction, while this section conducts the four-class classification experiments, including original images, histogram equalization, and two different gamma corrections. In order to test how close two $\gamma$ values can be distinguished by the proposed method, the following three cases are considered, and we use $\Delta\gamma = \gamma_2 - \gamma_1$ to show the closeness of the two gamma parameters: Case 1: $\gamma_1 < \gamma_2 < 1$, and $\gamma_1 = 0.50$, $\Delta\gamma = 0.10, 0.20, 0.30$; Case 2: $1 < \gamma_1 < \gamma_2$, and $\gamma_1 = 2.50$, $\Delta\gamma = 0.10, 0.30, 0.50$; Case 3: $\gamma_1 < 1 < \gamma_2$, and $\gamma_1 = 0.60, 0.70, 0.80$, $\gamma_2 = 1/\gamma_1$. The smaller $\Delta\gamma$ indicates the two gamma values are closer, and the classification difficulty increases accordingly. The result shown in Table IV indicates that our method

TABLE IV
EXPERIMENTAL RESULTS IN $CCPs$ CLASSIFYING ORIGINAL IMAGES, HISTOGRAM EQUALIZATION, AND TWO GAMMA CORRECTIONS IN THE SAME DATASET

| Case | $\Delta\gamma$ | $\gamma$ | | Dataset | | | | | |
|---|---|---|---|---|---|---|---|---|---|
| | | $\gamma_1$ | $\gamma_2$ | UCID | UCUS | COCO | MD | FR | MFC |
| Case 1 | 0.10 | 0.50 | 0.60 | 99.40 | 99.82 | 99.64 | 99.74 | 99.55 | 99.29 |
| | 0.20 | 0.50 | 0.70 | 99.59 | 99.88 | 99.64 | 99.75 | 99.58 | 99.28 |
| | 0.30 | 0.50 | 0.80 | 99.55 | 99.94 | 99.64 | 99.75 | 99.60 | 99.35 |
| Case 2 | 0.10 | 2.50 | 2.60 | 99.22 | 99.64 | 99.14 | 99.37 | 99.10 | 98.32 |
| | 0.30 | 2.50 | 2.80 | 99.22 | 99.64 | 99.18 | 99.38 | 99.13 | 98.40 |
| | 0.50 | 2.50 | 3.00 | 99.29 | 99.64 | 99.40 | 99.51 | 99.03 | 98.20 |
| Case 3 | 0.45 | 0.80 | 1.25 | 98.32 | 99.40 | 98.98 | 98.81 | 98.98 | 98.32 |
| | 0.73 | 0.70 | 1.43 | 99.07 | 99.64 | 99.22 | 99.12 | 99.28 | 98.55 |
| | 1.07 | 0.60 | 1.67 | 99.51 | 99.64 | 99.40 | 99.38 | 99.28 | 98.81 |

can discern different gamma corrections even the parameters of the two corrections are very close: in the experiment, even if $\Delta\gamma = 0.10$, classification accuracy remains very high. The visualization of the confusion matrix of the proposed classification method under the same dataset is shown in Fig. 9. It can be clearly seen that the diagonal value of the confusion matrix is much larger than other values, whether it is three or four-class classification results, which further proves the effectiveness and stability of the proposed method.

*2) Experiments Across Different Datasets:* Our method achieves good performance as the training and testing images are from the same dataset. However, given an image to be authenticated in realistic scenes, we do not know its origin. Therefore, we further test the proposed classification method when the training and testing set are from different datasets.

The three-class classification experiment includes the original images, the images after histogram equalization, and the gamma correction. According to Fig. 8, the classification performance of extreme gamma value is comparatively lower, so we performed three-class classification experiments when $\gamma = 0.20$ and $\gamma = 5.00$ in this section. The experimental results in Table V show that most of the classification results are greater than 97%, which indicates that the proposed method maintains good performance in different situations. When MFC is used as the testing set, the classification performance is relatively lower. It is because the image scenes in MFC dataset are more complicated, and the resolution

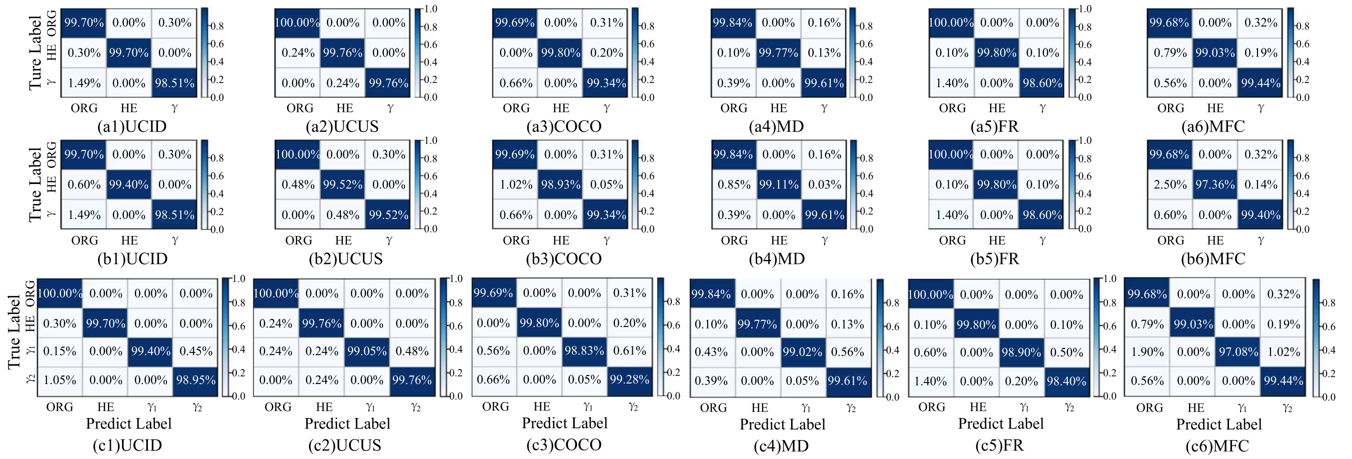


Fig. 9. Confusion matrix of the proposed classification method under the same dataset. From top to bottom: the three-class classification with gamma parameter 0.60; the three-class classification with gamma parameter 2.50; the four-class classification with gamma parameter 0.60 and 1.67.

of images is various, causing a slight drop in classification accuracy.

In order to further prove the versatility of the proposed classification method, the multi-class classification experiments, including original images, images after histogram equalization, and six different gamma corrections were carried out. We choose $\gamma = 1.67, 2.50, 5.00$ to be the parameter when $\gamma > 1$ and $\gamma = 0.30, 0.50, 0.70$ to be the parameter when $\gamma < 1$. The difficulty of the multi-class classification is greater than that of the three-class classification because of gamma parameters' diversity. The experimental results are shown in Table V, where most of the experimental results are higher than 97%. When the testing set is the MFC, the result drops slightly. This is also because the MFC dataset has complex image scenes and inconsistent resolution. The method yields satisfactory results, proving that the proposed method can distinguish various types of manipulated images and identify gamma corrections with different parameters.

*3) Experiments in the Wild:* To further demonstrate the effectiveness of this method, we choose to conduct experiments on three "in the wild" datasets. They are used in image classification and object recognition, other than tampering detection. The first dataset, MMPTRACK [30], comes from the recently proposed workshop and includes real images in different scenarios, with a resolution size of 640 × 360 and image format in JPEG format. The second dataset, VOC [31], comes from the "Visual Object Classes Challenge 2012" and includes different kinds of real images, with a resolution size from 320 × 240 to 331 × 500 and image format in JPEG format. The third dataset, VisDrone [32], comes from "Vision Meets Drones: A Challenge", and contains real images of different scenes captured by drones, with a resolution of 960 × 540 to 2000 × 1500, and the image format is JPEG. For these three datasets, we randomly selected 3000 images from different scenes and different categories to form three new datasets. In the experiment, the training set and the testing set are divided equally. The results are shown in Table VI, which keeps high accuracy in two and multi-class classification cases, proving the accuracy and stability of the proposed method, and is not affected by datasets. Furthermore, we studied the computational time and complexity of the classification method. The proposed method consists of two parts: feature extraction and feature classification. The time complexity of feature extraction is $O(n)$. Take images in MMPTRACK [30] for example, the average feature extraction time is 0.008 seconds for each image. Since SVM is used to classify features, the average classification time is 0.25 seconds.

*4) Comparative Experiments and Analysis:* The former sections verify the effectiveness, versatility, and the generalization ability of our classification method. This section compares the performance of the proposed classification method with several existing methods: Stamm and Liu [18], Akhtar and Khan [20], Cao *et al.* [22], and Singh *et al.* [33]. Since the existing detection methods are all two-class classification methods, distinguishing between original images and manipulated images, we conducted two-class classification, three-class classification, and four-class classification experiments. We evaluated based on the output of the relevant method. For example, Cao *et al.* [22] can discriminate original images and images after histogram equalization. As for gamma correction, we regarded it cannot produce correct classifications thus calculated as false results. The two-class classification experiment includes original images and histogram equalization. The three-class classification experiment includes original images, histogram equalization, and gamma correction with parameter 0.60 or 2.50, and the four-class classification experiment includes original images, histogram equalization, and two gamma corrections of parameter 0.60 and 2.50.

Because the fingerprint features of the original image and the image after histogram equalization are quite different, all the methods achieve good results in the two-class classification experiment. However, the proposed method has the advantage on multi-class classification tasks. Stamm and Liu [18] decide the weighted measure of the high-frequency components of the image histogram through the threshold. The histograms after different contrast enhancement operations have different high-frequency components, so they cannot be distinguished by a single threshold. Aktar and Khan [20] performed discrete

TABLE V

THREE-, MULTI-CLASS CLASSIFICATION RESULTS IN $CCPs$ ACROSS DIFFERENT DATASETS

| Test / Train | ORG+HE+GC | | | | | | | | | | | | ORG+HE+GC(six $\gamma$ below) | | | | | |
|---|---|---|---|---|---|---|---|---|---|---|---|---|---|---|---|---|---|---|
| | $\gamma$ = 0.20 | | | | | | $\gamma$ = 5.00 | | | | | | $\gamma$ = 0.30, 0.50, 0.70, 1.67, 2.50, 5.00 | | | | | |
| | UCID | UCUS | COCO | MD | FR | MFC | UCID | UCUS | COCO | MD | FR | MFC | UCID | UCUS | COCO | MD | FR | MFC |
| UCID | 98.26 | 99.13 | 97.77 | 97.43 | 97.20 | 95.49 | 98.90 | 98.57 | 97.36 | 97.78 | 97.70 | 95.68 | 99.23 | 99.14 | 98.60 | 98.72 | 98.70 | 97.11 |
| UCUS | 98.95 | 99.76 | 99.03 | 98.98 | 99.17 | 97.85 | 98.97 | 98.73 | 97.67 | 98.11 | 98.43 | 96.62 | 99.22 | 99.20 | 98.67 | 98.84 | 99.04 | 97.54 |
| COCO | 99.25 | 99.76 | 99.37 | 99.32 | 99.47 | 98.63 | 99.40 | 98.73 | 98.03 | 98.40 | 98.67 | 97.42 | 99.42 | 99.29 | 98.87 | 99.04 | 99.18 | 97.87 |
| MD | 99.25 | 99.76 | 99.44 | 99.36 | 99.53 | 98.63 | 99.40 | 98.73 | 98.08 | 98.45 | 98.80 | 97.45 | 99.44 | 99.32 | 98.91 | 99.08 | 99.23 | 97.89 |
| FR | 99.05 | 99.76 | 99.20 | 99.26 | 99.27 | 98.27 | 99.25 | 98.73 | 97.86 | 98.29 | 98.57 | 97.13 | 99.40 | 99.20 | 98.77 | 98.97 | 99.10 | 97.72 |
| MFC | 99.15 | 99.76 | 99.51 | 99.49 | 99.67 | 98.58 | 99.30 | 98.73 | 98.13 | 98.49 | 98.93 | 97.45 | 99.44 | 99.35 | 98.95 | 99.11 | 99.28 | 97.93 |

TABLE VI

TWO-, THREE- AND FOUR-CLASS CLASSIFICATION RESULTS IN $CCPs$ IN THE WILD DATASETS

| Dataset | ORG+HE | ORG+HE+GC | | |
|---|---|---|---|---|
| | | $\gamma$ = 0.60 | $\gamma$ = 2.50 | $\gamma$ = 0.60, 2.50 |
| MMPTRACK | 99.17 | 99.44 | 99.44 | 99.58 |
| VOC | 99.57 | 99.56 | 99.09 | 99.18 |
| VisDrone | 99.57 | 99.62 | 99.47 | 99.53 |

Fourier transform on the image histogram and extracted the difference between its DC coefficient and AC coefficient as a detection feature. Due to the large differences in the features obtained by different contrast enhancement manipulations, the manipulation type cannot be judged by a single threshold. Since Cao *et al.* [22] using the number of zero-gaps generated in the image histogram as the basis for judging contrast enhancement operations, and all the different types of contrast enhancement manipulations can lead to the generation of zero-gaps. So the type of contrast enhancement manipulation cannot be judged from the numbers alone. Singh *et al.* [33] performed Gaussian model fitting on the DC coefficients after DCT transformation of the image, but the obtained statistical parameter features could not fully reflect the traces left by different types of contrast enhancement manipulations. Therefore, its multi-classification results are not good. It can be seen from Table VII that in the three-class classification and four-class classification experiments, our method outperforms the comparative methods, achieving satisfactory results in the multi-classification tasks.

### C. Evaluations of Gamma Value Estimation

The gamma value estimation experiments on six datasets are carried out in this section. The parameter $\gamma$ starts from 0.20 to 0.80 with 0.10 steps when $\gamma < 1$. When $\gamma > 1$, the value is the reciprocal of the value taken when $\gamma < 1$. The estimation performance is evaluated in MSE defined as

$$MSE = \frac{1}{n}\sum_{i=1}^{n}\left(\hat{y}_i - y_i\right)^2. \tag{18}$$

The experimental results are shown in Table VIII. It can be seen that when $\gamma < 1$, the estimated value is more accurate. This is because the starting position and the maximum zero-gap span used to estimate the gamma value are more regular in this case. When $\gamma > 1$, the estimation performance is slightly lower, but the proposed method still has an acceptable performance.

### D. Robustness Analysis of the Classification Method

Our method achieves excellent classification performance in various scenarios and datasets and shows good generalization ability across the different datasets. In this section, we test its robustness against noise corruption, image filtering, and down-sampling attacks, as well as the effectiveness to different histogram equalization algorithms.

*1) Noise Attacks:* In this section, the proposed method is estimated under noise attack. The salt and pepper noise with zero mean was added to the MD dataset, and the variance is from 0.10 to 0.50. In order to observe the robustness under different $\gamma$ to a different amount of noise, we conducted three-class classification experiments, including original images, histogram equalization, and gamma correction. The value of gamma is 0.40, 0.60, 0.80, 2.00, 2.50, 3.00, 3.50, respectively. In each experiment, all images are added with the same amount of noise. From the experimental results shown in Fig. 10-(a), we can see that the experimental results are stable, and the proposed method achieves good performance, although the increase of noise brings a slight performance drop.

*2) Median Filter Attacks:* Median filtering is an operation that replaces the intensity of the central pixel with the median value of the pixels' intensities within the filter window. The effect of image median filtering depends on the size of the filtering window. Image forgers usually use median filtering to cover the traces left by local forgery manipulations. Due to the nature of the median filter, it only replaces the center pixel with the existing gray intensity so that no new gray intensity will be generated. Therefore, the zero-gaps in the operated image's histogram still exist after median filtering. Because of the property, the proposed fingerprint feature, which calculates the span of two zero-gaps in the histogram, is robust to the median filtering. The four-class classification experiments, which include original images, histogram equalization, and the gamma correction with parameters 0.60 and 2.50 was conducted. Fig. 10-(b) records the classification results of each dataset in different sizes of filtering windows. It can be seen from the experimental results that as the window size increases, the classification results show a very slight downward trend, which indicates that the filter window size only has a slight impact on the extraction of fingerprint

TABLE VII

COMPARISONS BETWEEN THE OUR CLASSIFICATION METHOD AND THE EXISTING DETECTION METHODS IN TWO-, THREE-, AND FOUR-CLASS CLASSIFICATIONS IN $CCPs$

| Dataset | ORG+HE | | | | | ORG+HE+GC($\gamma$ = 0.60) | | | | | ORG+HE+ GC($\gamma$ = 2.50) | | | | | ORG+HE+GC($\gamma$ = 0.60, 2.50) | | | | |
|---|---|---|---|---|---|---|---|---|---|---|---|---|---|---|---|---|---|---|---|---|
| | Stamm | Aktar | Cao | Singh | Ours | Stamm | Aktar | Cao | Singh | Ours | Stamm | Aktar | Cao | Singh | Ours | Stamm | Aktar | Cao | Singh | Ours |
| UCID | 99.88 | 98.80 | **100** | 94.69 | 99.10 | 65.92 | 65.87 | 66.67 | 61.53 | **99.30** | 65.92 | 65.87 | 66.67 | 61.53 | **99.20** | 49.44 | 49.40 | 50.00 | 43.91 | **99.33** |
| UCUS | 95.83 | 95.71 | **100** | 92.74 | **100** | 63.89 | 63.81 | 66.67 | 59.05 | **99.84** | 63.89 | 63.81 | 66.67 | 62.22 | **99.68** | 47.92 | 47.86 | 50.00 | 45.83 | **99.64** |
| COCO | 97.68 | 98.85 | **99.77** | 94.00 | 99.51 | 65.12 | 65.90 | 66.51 | 61.99 | **99.61** | 65.12 | 65.90 | 66.51 | 59.74 | **99.32** | 48.84 | 49.43 | 49.89 | 44.36 | **99.44** |
| MD | 97.69 | 98.41 | **99.77** | 94.09 | 99.72 | 65.12 | 65.61 | 66.51 | 62.19 | **99.59** | 65.12 | 65.61 | 66.51 | 50.71 | **98.58** | 48.84 | 49.20 | 49.89 | 39.46 | **99.38** |
| FR | 95.85 | 97.70 | **99.75** | 92.75 | 99.30 | 63.90 | 65.13 | 66.50 | 61.87 | **99.47** | 63.90 | 65.13 | 66.50 | 55.07 | **99.20** | 47.93 | 48.85 | 49.88 | 36.55 | **99.28** |
| MFC | 96.15 | 97.31 | **99.61** | 95.71 | 99.56 | 64.10 | 64.88 | 66.40 | 62.85 | **99.38** | 64.10 | 64.88 | 66.40 | 46.49 | **98.81** | 48.08 | 48.66 | 49.80 | 31.45 | **98.81** |

TABLE VIII

EVALUATIONS OF GAMMA VALUE ESTIMATION IN $MSE$ ON SIX DATASETS

| Dataset | $\gamma < 1$ | | | | | | | $\gamma > 1$ | | | | | | |
|---|---|---|---|---|---|---|---|---|---|---|---|---|---|---|
| | 0.20 | 0.30 | 0.40 | 0.50 | 0.60 | 0.70 | 0.80 | 1.25 | 1.43 | 1.67 | 2.00 | 2.50 | 3.33 | 5.00 |
| UCID | 0.0003 | 0.0067 | 0.0050 | 0.0043 | 0.0047 | 0.0033 | 0.0044 | 0.2395 | 0.0067 | 0.2482 | 0.0166 | 0.1143 | 0.2162 | 0.0453 |
| UCUS | 0.0003 | 0.0018 | 0.0061 | 0.0001 | 0.0002 | 0.0002 | 0.0042 | 0.2251 | 0.0010 | 0.1796 | 0.0257 | 0.1086 | 0.1581 | 0.0563 |
| COCO | 0.0003 | 0.0010 | 0.0002 | 0.0001 | 0.0002 | 0.0002 | 0.0005 | 0.2275 | 0.0031 | 0.2083 | 0.0219 | 0.1201 | 0.1892 | 0.0530 |
| MD | 0.0003 | 0.0022 | 0.0021 | 0.0009 | 0.0011 | 0.0008 | 0.0019 | 0.2313 | 0.0039 | 0.2187 | 0.0204 | 0.1175 | 0.1979 | 0.0504 |
| FR | 0.0003 | 0.0021 | 0.0002 | 0.0001 | 0.0002 | 0.0002 | 0.0030 | 0.2108 | 0.0003 | 0.1569 | 0.0305 | 0.1121 | 0.1038 | 0.0667 |
| MFC | 0.0133 | 0.0100 | 0.0029 | 0.0025 | 0.0030 | 0.0022 | 0.0056 | 0.2178 | 0.0038 | 0.2101 | 0.0220 | 0.1215 | 0.2344 | 0.0618 |

features. On the whole, the proposed fingerprint feature shows robustness to median filtering.

*3) Down-Sampling Attacks:* In order to verify the effectiveness of the proposed method on low-resolution images, we performed a down-sampling operation using bicubic interpolation on six datasets. We then performed four-class classification experiments, including original images, histogram equalization, and the gamma correction with parameters of 0.60 and 2.50. Fig 10-(c) records the classification results of each dataset at different image resolutions. The experimental results show that the classification result shows a downward trend with the decrease of the resolution, which indicates that the image resolution influences the fingerprint feature. It is because decreasing image resolution decreases image pixels, which increases the number of zero-gaps in the original image. It finally reduces the difference of fingerprint feature distribution of the image before and after the contrast enhancement manipulations, so $CCPs$ decrease.

*4) Effectiveness to Different Histogram Equalizations:* Histogram equalization is one of the most popular enhancement techniques to improve the visual perception of an image. The advantage of histogram equalization is its simplicity with reasonably good results. The experiments above contain this simple histogram equalization manipulation. However, due to excessive stretching of the intensity distribution of the histogram, various artifacts such as saturation and halo artifacts will be introduced. Therefore, various attempts have been made to overcome the shortcomings of histogram equalization. These algorithms try to enhance the contrast while retaining the average brightness of the original image. In general, these algorithms divide the original histogram into sub-histograms and equalize each division independently, such as Bi-histogram Equalization (BBHE) [34],

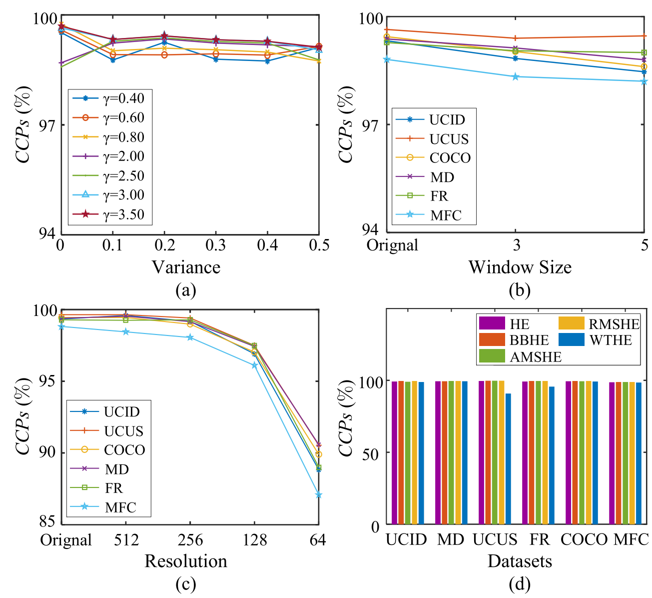


Fig. 10. Robustness of the classification method. (a) The noise attack results under the classification of original images, histogram equalization, and gamma correction with different parameter $\gamma$ on the MD dataset. (b) The median filtering attack under the classification, including original images, histogram equalization, and gamma correction with 0.60 and 2.50 on different datasets. The window size is $3 \times 3$ and $5 \times 5$. (c) The down-sampling attack under the classification including original images, histogram equalization, and gamma correction with 0.60 and 2.50 on different datasets. The resolution is $512 \times 512$, $256 \times 256$, $128 \times 128$, and $64 \times 64$. (d) The classification accuracy in $CCPs$ of four-class classification experiments includes original images, a type of histogram equalization, and the gamma correction with 0.60 and 2.50. The histogram equalization methods include the simple histogram equalization and four types of the modified histogram equalization.

which divides the histogram at the mean intensity; Recursive Mean-separated Histogram Equalization (RMSHE) [35], which uses BBHE [34] recursively to preserve the original

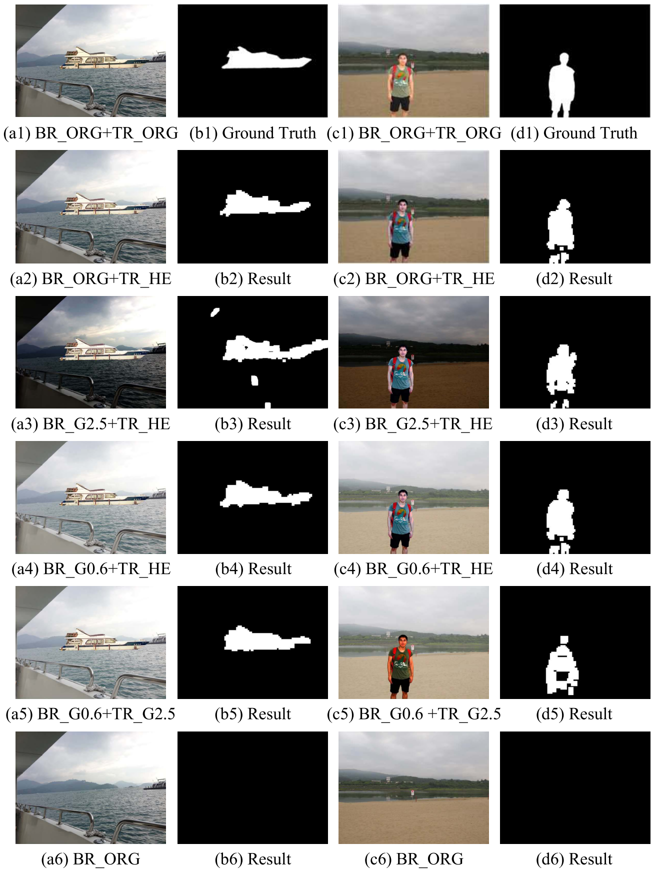


Fig. 11. Localization of splicing images. BR: background region; TR: target region; G0.6: gamma correction $\gamma = 0.60$; G2.5: gamma correction $\gamma = 2.50$.

mean intensity; Adaptive Modified Histogram Equalization (AMHE) [36], which scales the magnitudes of the probability density function of the original image before equalization and the scale factor is determined adaptively based on the mean brightness of the original image; Weighted Thresholded Histogram Equalization (WTHE) [37], which modifies the probability distribution function of an image before histogram equalization.

To prove that the proposed classification method can distinguish not only the simple histogram equalization but also the modified histogram equalization methods, we performed the contrast enhancement manipulations on six datasets, including the simple histogram equalization, the modified histogram equalization, and gamma correction with 0.60 and 2.50. Then the four-class classification experiments were carried out, including original images, a type of histogram equalization method, and gamma correction with 0.60 and 2.50. The experimental results shown in Fig. 10-(d) indicate that the proposed classification method can distinguish the modified histogram equalization successfully.

### *E. Application to Image Authentication*

The experiments conducted so far are detections of global image forgeries. However, our method can also detect and localize specific regional splicing forgery. An example of a splicing forgery is shown in Fig. 11. The spliced regions are all derived from the image after histogram equalization or gamma correction before it is inserted into an unaltered or contrast-enhanced image. Fig. 11 respectively lists two examples of splicing forgery detection. To localize the forgery, the input image is segmented into blocks, and the ZGS fingerprint of each block is calculated. Then we calculate the number of spans between the two non-zero values in the ZGS fingerprint in each block and select an appropriate threshold for classification. The results of block-wise detection on the forged images under different contrast enhancement manipulations are shown in Fig. 11-(b2)$\sim$(b5) and (d2)$\sim$(d5). As the result shows, some false alarms occur. It is because forgery localization requires features to have a higher ability to distinguish between the tampered region and the non-tampered region. For example, when the gamma is less than one, it is difficult to distinguish the original region from the tampered region when the image is divided into blocks because of the weak mapping of power function and the longer span between zero-gaps. The last row of Fig. 11 shows some examples of original images. The experiment was conducted with the parameters used in location detection of the tampered images in the experiment, and there is no false alert response in the detection results. The method proposed in this paper can detect and localize splicing forgery in some cases.

## V. Conclusion

In this article, we proposed a simple universal method to detect various contrast enhancement manipulations. By analyzing the traces these manipulations left on the histograms of the images, we propose ZGS as the only feature to discriminate various contrast enhancement manipulations. Furthermore, we improve its performance by using adaptive effective range selection process. Our detection method not only can distinguish the manipulated images with different contrast enhancement manipulations from the original images but also can identify which type of contrast enhancement manipulation is applied to the image. Meanwhile, it can identify the gamma correction with different parameters and determine its value. Moreover, it can handle the simple histogram equalization and the modified histogram equalization techniques and locate the regions with different contrast enhancement manipulations in splicing forged images. Experimental results indicate that the proposed detection method achieves a good performance under different contrast enhancement manipulations.

Although our method demonstrates robustness to noise attacks (such as salt and pepper noise), it is worth noting that the proposed detection method is not robust enough to JPEG compression. This is because our method is based on zero gaps in the image histogram, and the JPEG compression causes zero gaps to disappear. Then the zero-gap span features extracted cannot fully reflect the traces of contrast enhancement, which eventually leads to the decline of the classification performance. Other attacks combined with JPEG compression can also cause this problem. In follow-up work, we will improve its robustness to JPEG compression.

## REFERENCES


[1] T. Liu and X. Yuan, "Adaptive feature calculation and diagonal mapping for successive recovery of tampered regions," *IEEE Trans. Circuits Syst. Video Technol.*, vol. 31, no. 7, pp. 2617–2630, Jul. 2021.

[2] G.-S. Lin, M.-K. Chang, and Y.-L. Chen, "A passive-blind forgery detection scheme based on content-adaptive quantization table estimation," *IEEE Trans. Circuits Syst. Video Technol.*, vol. 21, no. 4, pp. 421–434, Apr. 2011.

[3] A. Ferreira *et al.*, "Behavior knowledge space-based fusion for copy–move forgery detection," *IEEE Trans. Image Process.*, vol. 25, no. 10, pp. 4729–4742, Oct. 2016.

[4] X. Zhao, S. Wang, S. Li, and J. Li, "Passive image-splicing detection by a 2-D noncausal Markov model," *IEEE Trans. Circuits Syst. Video Technol.*, vol. 25, no. 2, pp. 185–199, Feb. 2015.

[5] T. J. de Carvalho, C. Riess, E. Angelopoulou, H. Pedrini, and A. Rocha, "Exposing digital image forgeries by illumination color classification," *IEEE Trans. Inf. Forensics Security*, vol. 8, no. 7, pp. 1182–1194, Jul. 2013.

[6] Y. Zhang, G. Zhu, L. Wu, S. Kwong, H. Zhang, and Y. Zhou, "Multi-task SE-network for image splicing localization," *IEEE Trans. Circuits Syst. Video Technol.*, vol. 32, no. 7, pp. 4828–4840, Jul. 2022.

[7] H. Li, W. Luo, X. Qiu, and J. Huang, "Identification of various image operations using residual-based features," *IEEE Trans. Circuits Syst. Video Technol.*, vol. 28, no. 1, pp. 31–45, Jan. 2018.

[8] V. Conotter, P. Comesana, and F. Perez-Gonzalez, "Joint detection of full-frame linear filtering and JPEG compression in digital images," in *Proc. IEEE Int. Workshop Inf. Forensics Secur. (WIFS)*, Nov. 2013, pp. 156–161.

[9] X. Kang, M. C. Stamm, A. Peng, and K. J. R. Liu, "Robust median filtering forensics using an autoregressive model," *IEEE Trans. Inf. Forensics Security*, vol. 8, no. 9, pp. 1456–1468, Sep. 2013.

[10] C. Chen, J. Ni, and J. Huang, "Blind detection of median filtering in digital images: A difference domain based approach," *IEEE Trans. Image Process.*, vol. 22, no. 12, pp. 4699–4710, Dec. 2013.

[11] Y. Zhang, S. Li, S. Wang, and Y. Q. Shi, "Revealing the traces of median filtering using high-order local ternary patterns," *IEEE Signal Process. Lett.*, vol. 21, no. 3, pp. 275–279, Mar. 2014.

[12] T. Bianchi and A. Piva, "Image forgery localization via block-grained analysis of JPEG artifacts," *IEEE Trans. Inf. Forensics Security*, vol. 7, no. 3, pp. 1003–1017, Jun. 2012.

[13] P. Ferrara, T. Bianchi, A. D. Rosa, and A. Piva, "Reverse engineering of double compressed images in the presence of contrast enhancement," in *Proc. IEEE 15th Int. Workshop Multimedia Signal Process. (MMSP)*, Sep. 2013, pp. 141–146.

[14] F. Huang, J. Huang, and Y. Q. Shi, "Detecting double JPEG compression with the same quantization matrix," *IEEE Trans. Inf. Forensics Security*, vol. 5, no. 4, pp. 848–856, Dec. 2010.

[15] J. Lukáš and J. Fridrich, "Estimation of primary quantization matrix in double compressed jpeg images," in *Proc. Digit. Forensic Res. Workshop*, 2003, pp. 5–8.

[16] V. Conotter, P. Comesana, and F. Pérez-González, "Forensic detection of processing operator chains: Recovering the history of filtered JPEG images," *IEEE Trans. Inf. Forensics Security*, vol. 10, no. 11, pp. 2257–2269, Nov. 2015.

[17] A. C. Popescu and H. Farid, "Statistical tools for digital forensics," in *Proc. Int. Workshop Inf. Hiding*. Cham, Switzerland: Springer, 2004, pp. 128–147.

[18] M. C. Stamm and K. J. R. Liu, "Forensic detection of image manipulation using statistical intrinsic fingerprints," *IEEE Trans. Inf. Forensics Security*, vol. 5, no. 3, pp. 492–506, Sep. 2010.

[19] H.-D. Yuan, "Identification of global histogram equalization by modeling gray-level cumulative distribution," in *Proc. IEEE China Summit Int. Conf. Signal Inf. Process.*, Jul. 2013, pp. 645–649.

[20] Z. Akhtar and E. Khan, "Revealing the traces of histogram equalisation in digital images," *IET Image Process.*, vol. 12, no. 5, pp. 760–768, May 2018.

[21] G. Cao, Y. Zhao, and R. Ni, "Forensic estimation of gamma correction in digital images," in *Proc. IEEE Int. Conf. Image Process.*, Sep. 2010, pp. 2097–2100.

[22] G. Cao, Y. Zhao, R. Ni, and X. Li, "Contrast enhancement-based forensics in digital images," *IEEE Trans. Inf. Forensics Security*, vol. 9, no. 3, pp. 515–525, Mar. 2014.

[23] G. B. Thomas and R. L. Finney, *Calculus*. Reading, MA, USA: Addison-Wesley, 1961.

[24] C. C. Chang and C. J. Lin, "LIBSVM: A library for support vector machines," *ACM Trans. Intell. Syst. Technol.*, vol. 2, no. 3, pp. 1–27, 2011.

[25] G. Schaefer and M. Stich, "UCID: An uncompressed color image database," *Proc. SPIE*, vol. 5307, pp. 472–480, Dec. 2003.

[26] K. Wattanachote, T. K. Shih, W.-L. Chang, and H.-H. Chang, "Tamper detection of jpeg image due to seam modifications," *IEEE Trans. Inf. Forensics Security*, vol. 10, no. 12, pp. 2477–2491, Dec. 2015.

[27] T. Y. Lin, M. Maire, S. Belongie, J. Hays, and C. L. Zitnick, *Microsoft Coco: Common Objects in Context*. Cham, Switzerland: Springer, 2014.

[28] V. V. Kniaz, V. Knyaz, and F. Remondino, "The point where reality meets fantasy: Mixed adversarial generators for image splice detection," in *Proc. Adv. Neural Inf. Process. Syst.*, 2019, pp. 215–226.

[29] H. Guan *et al.*, "MFC datasets: Large-scale benchmark datasets for media forensic challenge evaluation," in *Proc. IEEE Winter Appl. Comput. Vis. Workshops (WACVW)*, Jan. 2019, pp. 63–72.

[30] X. Han *et al.*, "MMPTRACK: Large-scale densely annotated multi-camera multiple people tracking benchmark," 2021, *arXiv:2111.15157*.

[31] M. Everingham, L. Van Gool, C. K. I. Williams, J. Winn, and A. Zisserman. (2012). *The PASCAL Visual Object Classes Challenge 2012 (VOC2012) Results*. [Online]. Available: http://www.pascal-network.org/challenges/VOC/voc2012/workshop/index.html

[32] P. Zhu *et al.*, "Detection and tracking meet drones challenge," *IEEE Trans. Pattern Anal. Mach. Intell.*, early access, Oct. 14, 2021, doi: 10.1109/TPAMI.2021.3119563.

[33] N. Singh, A. Gupta, and R. C. Jain, "Adaptive histogram equalization based image forensics using statistics of DC dct coefficients," *Adv. Electr. Electron. Eng.*, vol. 16, no. 1, pp. 125–134, 2018.

[34] Y.-T. Kim, "Contrast enhancement using brightness preserving bi-histogram equalization," *IEEE Trans. Consum. Electron.*, vol. 43, no. 1, pp. 1–8, Feb. 1997.

[35] S.-D. Chen and A. R. Ramli, "Contrast enhancement using recursive mean-separate histogram equalization for scalable brightness preservation," *IEEE Trans. Consum. Electron.*, vol. 49, no. 4, pp. 1301–1309, Nov. 2003.

[36] H.-J. Kim, J.-M. Lee, J.-A. Lee, S.-G. Oh, and W.-Y. Kim, "Contrast enhancement using adaptively modified histogram equalization," in *Proc. Pacific-Rim Symp. Image Video Technol.* Cham, Switzerland: Springer, 2006, pp. 1150–1158.

[37] Q. Wang and R. K. Tan, "Fast image/video contrast enhancement based on weighted thresholded histogram equalization," *IEEE Trans. Consum. Electron.*, vol. 53, no. 2, pp. 757–764, May 2007.


**Xiuli Bi** received the B.Sc. and M.Sc. degrees from Shanxi Normal University, China, in 2004 and 2007, respectively, and the Ph.D. degree in computer science from the University of Macau, in 2017. She is currently an Associate Professor with the College of Computer Science and Technology, Chongqing University of Posts and Telecommunications, China. Her research interests include image processing, multimedia security, and forensic.

**Yixuan Shang** received the B.S. degree in computer science and technology from the Nanyang Institute of Technology, China, in 2019. She is currently pursuing the M.S. degree in computer science and technology with the Chongqing University of Posts and Telecommunications, China. Her research interests include image processing, multimedia security, and forensic.

**Bo Liu** (Member, IEEE) received the B.B.M. degree from the Department of Information Technology, University of International Relations, China, in 2010, and the M.Sc. and Ph.D. degrees from the Department of Computer and Information Science, University of Macau, Macao, China, in 2014 and 2020, respectively. He is currently a Lecturer with the School of Computer Science and Technology, Chongqing University of Posts and Telecommunications, China. His current research interests include multimedia forensics, image processing, and computer vision.

**Bin Xiao** received the B.S. and M.S. degrees in electrical engineering from Shanxi Normal University, Xi'an, China, in 2004 and 2007, respectively, and the Ph.D. degree in computer science from Xidian University, Xi'an. He is currently a Professor with the Chongqing University of Posts and Telecommunications, Chongqing, China. His research interests include image processing and pattern recognition.

**Weisheng Li** (Member, IEEE) received the B.S. and M.S. degrees from the School of Electronics and Mechanical Engineering, Xidian University, Xi'an, China, in July 1997 and July 2000, respectively, and the Ph.D. degree from the School of Computer Science and Technology, Xidian University, in July 2004. He is currently a Professor with the Chongqing University of Posts and Telecommunications. His research interests include intelligent information processing and pattern recognition.

**Xinbo Gao** (Senior Member, IEEE) received the B.Eng., M.Sc., and Ph.D. degrees in signal and information processing from Xidian University, Xi'an, China, in 1994, 1997, and 1999, respectively. From 1997 to 1998, he was a Research Fellow with the Department of Computer Science, Shizuoka University, Shizuoka, Japan. From 2000 to 2001, he was a Postdoctoral Research Fellow with the Department of Information Engineering, The Chinese University of Hong Kong, Hong Kong. From 2001 to 2020, he was with the School of Electronic Engineering, Xidian University. Since 2020, he has been the President of the Chongqing University of Posts and Telecommunications, Chongqing, China. He has published five books and approximately 200 technical articles in refereed journals and proceedings, including the IEEE Transactions on Image Processing, the IEEE Transactions on Neural Networks and Learning Systems, the IEEE Transactions on Circuits and Systems for Video Technology, the IEEE Transactions on Systems, Man, and Cybernetics, the *International Journal of Computer Vision*, and *Pattern Recognition* in the below areas. His current research interests include multimedia analysis, computer vision, pattern recognition, machine learning, and wireless communications. He is a fellow of the Institution of Engineering and Technology. He has served as the general chair/co-chair, the program committee chair/co-chair, or a PC member for approximately 30 major international conferences. He is on the Editorial Boards of several journals, including *Signal Processing* (Elsevier) and *Neurocomputing* (Elsevier).